DOI 10.1007/s11223-019-00066-9
Strength of Materials, Vol. 51, No. 2, March, 2019

FRACTURE BEHAVIOR OF SINGLE-CRYSTAL ALLOYS UNDER THERMOCYCLIC LOADING

L. B. Getsov,[a,1] A. S. Semenov,[b,2] A. N. Grudinin,[b] and A. I. Rybnikov[a]

UDC 539.421, 620.178.3

Experimental study results for thermal fatigue fracture of sand-glass specimens from a ZhS32 single-crystal alloy with different crystallographic orientations are presented over a wide range of maximum and minimum cycle temperature variations. Crystallographic, fractographic, and finite element data were used to identify crystallographic and noncrystallographic fracture modes of a single-crystal alloy. The noncrystallographic mode is realized at high maximum cycle temperatures and comparatively narrow temperature ranges. It is characterized by mode I crack growth. The crystallographic mode is realized at lower maximum temperatures and a wide range of cycle temperature variations. It is characterized by combined I–II mode crack growth in crystallographic plane {111}. The chart of fracture mechanisms in the maximum temperature-temperature range coordinates is proposed. The boundary between the regions permits of approximation, corresponding to the Arrhenius equation.

Keywords: single-crystal alloy, thermal fatigue, crystallographic and noncrystallographic fracture modes, crack, finite element simulation.

Introduction. Experimental and theoretical studies on the crack resistance of heat-resistant single-crystal nickel-base alloys become currently central due to their ever-widening application in the manufacture of modern aircraft gas turbine engine blades [1, 2].

Fatigue cracks in those alloys can extend over the crystallographic planes and over the surfaces with an externally affected orientation (similar to isotropic polycrystalline materials). Corresponding crystallographic and noncrystallographic fracture modes, as was shown in [3–7], are dependent on temperature, mechanical effects, frequency and loading conditions, and on the environment.

At low temperatures and high stress intensity factors the crack grows in crystallographic plane {111}. At high temperatures and low stress intensity factors, a mode I crack extends in the plane, differing from the crystallographic one and determined by maximum circumferential stresses in the vicinity of the crack tip (in the simplest case of uniaxial loading, in the plane with the normal oriented along the load line).

The object of the present study is to assess the conditions of origin of crystallographic and noncrystallographic fracture modes of single-crystal alloys on thermal fatigue fracture and the generalize high-cycle fatigue results [3–7, etc.] for the thermal fatigue case.

The effect of the crystallographic orientation (CGO) of a ZhS36 single-crystal alloy and loading conditions on thermal fatigue fracture modes was analyzed earlier in [8]. Unfortunately, experiments performed on a ZhS36 alloy with orientations $\langle 001 \rangle$, $\langle 011 \rangle$, and $\langle 111 \rangle$ were not numerous. The relations demonstrated only the fracture patterns against the cycle temperature parameters. Provision of more stringent quantitative boundary conditions for

[a]Polzunov Power Equipment Research & Design Science & Technology Association, Saint Petersburg, Russia ([1]guetsov@yahoo.com). [b]Peter the Great Saint Petersburg State Polytechnic University, Saint Petersburg, Russia ([2]semenov.artem@googlemail.com). Translated from Problemy Prochnosti, No. 2, pp. 36 – 50, March – April, 2019. Original article submitted April 23, 2018.

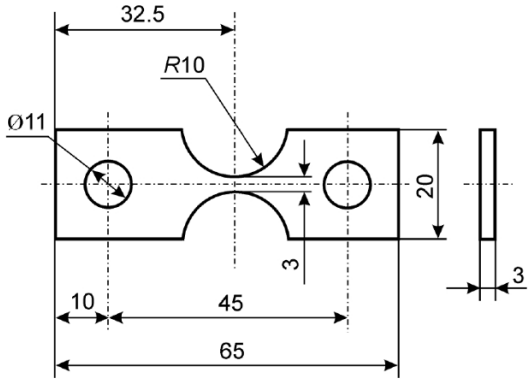

Fig. 1. Specimen for thermal fatigue tests.

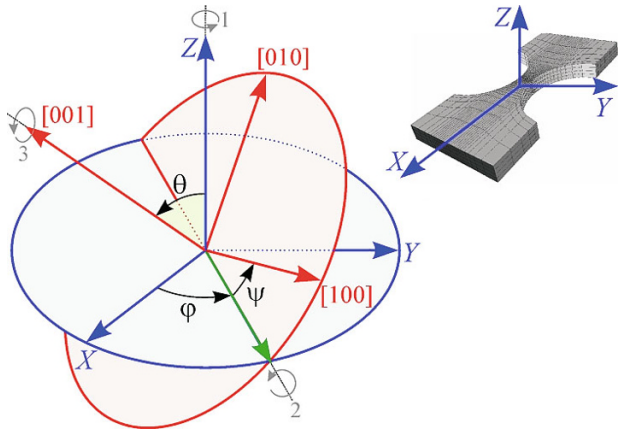

Fig. 2. Euler angles for setting the crystallographic orientation of the specimen.

the fracture modes (charts of fracture mechanisms) is of importance for this information to be used in defining deformation fracture criterion parameters [8–10] as well as in simulating thermal fatigue crack growth [11].

In the present study, an effort was made to plot the charts (diagrams) of fracture mechanisms (modes) under thermocyclic loading of ZhS32 single-crystal alloy specimens [12].

Specimens and Test Conditions. Rigidly fixed sand-glass specimens 3 mm thick with one polished surface were the object of investigation (Fig. 1). The tests were performed at cyclic temperature variations within a preset range $T_{\min} - T_{\max}$ in vacuum, thus, the formation of slip bands and crack nucleation can be followed and their growth rate on the polished surface (×250 magnification) is evaluated. The procedure of thermal fatigue tests is detailed in [13, 14].

Heating of the specimens was effected with current passage. They were fixed on the heads with the bolted joint in a special device. The tests were carried out at different maximum ($T_{\max} = 900$–1100°C) and minimum ($T_{\min} = 200$–700°C) cycle temperatures. A part of the specimens was held at $T_{\max}$ for 2 min.

The specimens were subjected to thermal pretreatment under special conditions (condition 1): homogenization at $T = 1285$°C, 1 h 30 min, cooling rate above 100°/min, ageing at 1000°C for 6 h and under standard conditions (condition 2): homogenization at $T = 1270$°C, 1 h 15 min, cooling rate 40–80°/min, ageing at 1000°C for 6 h [15].

The chemical composition (%) of a ZhS32 single-crystal alloy used for specimen preparing: 0.12–0.18 C, 4.3–5.6 Cr, 8.0–10.0 Co, 0.8–1.4 Mo, 7.7–9.5 W, 3.5–4.5 Ta, 3.5–4.5 Re, 1.4–1.8 Nb, 5.6–6.3 Al, Ni base.

Crystallographic Orientation of the Specimens. The specimens exhibited different axial and azimuthal orientations. The deflection of axial orientation from orientation $\langle 100 \rangle$ varied within 0–40°. The crystallographic orientation, characterized by the three Euler angles φ, θ, ψ (Fig. 2), was evaluated with the Laue pattern taken for each specimen (Fig. 3), the angles φ, θ, ψ and Schmid factor were calculated by the following procedure.

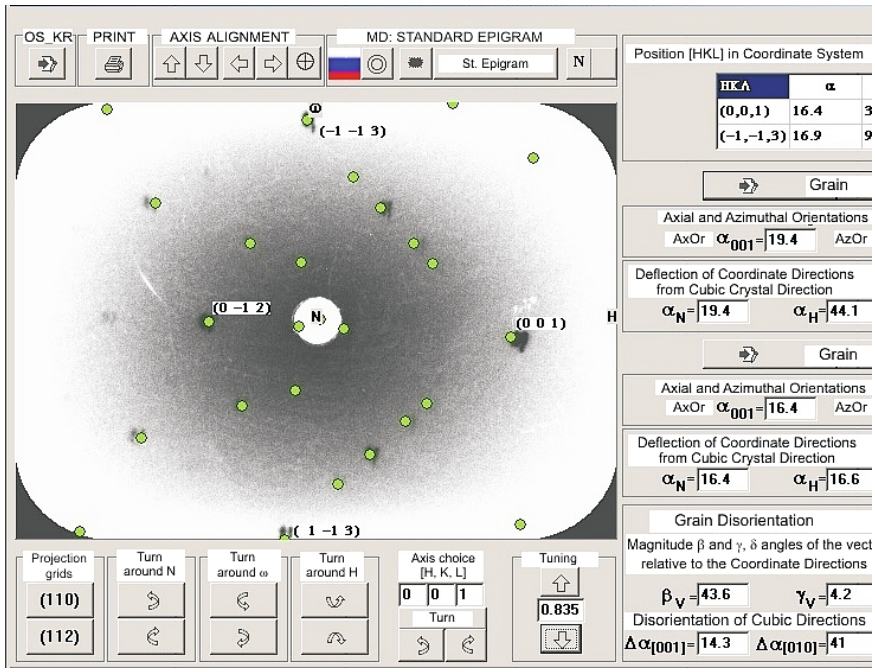

Fig. 3. Data processing with the Laue pattern.

1. X-ray diffraction (Laue pattern) results were used to determine the three angles α_X, α_Y, α_Z, characterizing the deflection of the laboratory system of coordinates (X, Y, Z), related to the specimen, from the crystallographic system of coordinates [100], [010], [001].

2. With the angles α_X, α_Y, and α_Z, the three Euler angles φ, θ, and ψ are defined by the formulae

$$\begin{cases} \varphi = \dfrac{1}{2}\left(\pm \arccos \dfrac{\cos\alpha_X + \cos\alpha_Y}{1+\cos\alpha_Z} \pm \arccos \dfrac{\cos\alpha_X - \cos\alpha_Y}{1-\cos\alpha_Z} \right), \\ \theta = \pm\alpha_Z, \\ \psi = \dfrac{1}{2}\left(\pm \arccos \dfrac{\cos\alpha_X + \cos\alpha_Y}{1+\cos\alpha_Z} \mp \arccos \dfrac{\cos\alpha_X - \cos\alpha_Y}{1-\cos\alpha_Z} \right). \end{cases} \quad (1)$$

3. With the Euler angles φ, θ, ψ, the matrix A_{ij} of basis rotation from the laboratory system of coordinates to the crystallographic one is defined

$$A_{ij} = \begin{bmatrix} \cos\psi\cos\varphi - \sin\psi\cos\theta\sin\varphi & \cos\psi\sin\varphi + \sin\psi\cos\theta\cos\varphi & \sin\psi\sin\theta \\ -\sin\psi\cos\varphi - \cos\psi\cos\theta\sin\varphi & -\sin\psi\sin\varphi + \cos\psi\cos\theta\cos\varphi & \cos\psi\sin\theta \\ \sin\theta\sin\varphi & -\sin\theta\cos\varphi & \cos\theta \end{bmatrix}. \quad (2)$$

4. Based on the matrix A_{ij}, the Schmid factor λ is determined with the assumption of the load acting along the X axis of the laboratory system of coordinates

$$\lambda = \frac{A_{i1} n_i}{\sqrt{n_k n_k}} \frac{A_{j1} l_j}{\sqrt{l_m l_m}}, \quad (3)$$

where n_i is the coordinates of the normal to the slip plane (hkl) set in the crystallographic basis ($n_1 = h$, $n_2 = k$, $n_3 = l$), l_j is the coordinates of the slip direction vector [hkl] set in the crystallographic basis ($l_1 = h$, $l_2 = k$, $l_3 = l$).

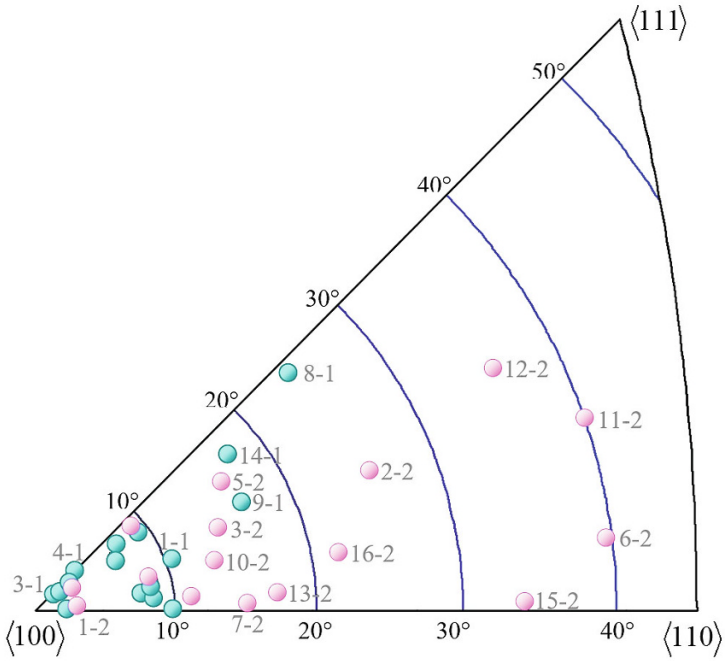

Fig. 4. Axial orientation of examined specimens: (●) condition 1, (○) condition 2.

5. The slip line slopes formed by the slip planes (with the normal n_i) on the OXY and OXZ surfaces of the specimen were also derived from the matrix A_{ij}

$$\cos\xi_{OXY} = \frac{A_{i2}n_i}{\sqrt{n_k n_k - (A_{j3}n_j)^2}},$$
$$\cos\xi_{OXZ} = \frac{-A_{i3}n_i}{\sqrt{n_k n_k - (A_{j2}n_j)^2}}. \quad (4)$$

The axial orientation of all examined specimens with differentiation of thermal treatment conditions is shown in Fig. 4. The Euler angles (1), maximum Schmid factors for all slip systems (3), deflections of specimen axes from orientation ⟨100⟩ are summarized in Table 1 for all examined specimens treated under conditions 1 and 2.

These parameters, the rotation matrices A_{ij}, and slip line slopes on the specimen surfaces were calculated by the above procedure with the CES (Constitutive Equation Studio) program [16].

Fractographic Results. Fracture modes of each specimen were identified with regard to the relations of slip line slopes on the surfaces (4) and Schmid factors (3) as well as individual CGO data. For verifying the appearance of a noncrystallographic mode, the stress data were also used, obtained with finite element simulation, examined below. For identifying crystallographic and mixed fracture modes, fractographic results for specimen fractures were used that also permit of establishing the evolutionary nature of fracture and its stage-by-state development. Fractographic examination was perfomed on TESCAN and JEOL scanning electron microscopes.

Fractographic results are summarized in Tables 2* and 3*. As a rule, the fracture zone of specimens consists of a crack nucleus (or several nuclei) where the crack originates by the crystallographic mode over one of the slip planes, retarded growth zones (RGZ) of the crack (crystallographic or noncrystallographic), and accelerated growth zone (AGZ) of the crack (final rupture).

In some cases, the fusion zone is observed on the last section of the diagram that is due to short-term local overheating since the thermocouple controlling temperature was located at a distance from the final rupture.

* The data are obtained with the assistance of E. A. Tikhomirova.

TABLE 1. Crystallographic Orientation and Schmid Factors for Single-Crystal Specimens

Specimen No.	Axial deflection, deg	φ, deg	θ, deg	ψ, deg	λ_{max}	Slip system with λ_{max}
1-1	10.4	7.0	32.2	3.8	0.4653	(−1 1 1) [1 0 1]
2-1	9.4	12.5	36.4	−4.3	0.4501	(1 1 1) [1 −1 0]
3-1	2.5	3.8	21.7	−1.5	0.4223	(−1 1 1) [1 0 1]
4-1	7.4	20.8	13.4	−14.5	0.4422	(−1 1 1) [1 0 1]
5-1	7.8	16.6	28.0	−13.5	0.4559	(1 1 1) [1 −1 0]
6-1	9.9	69.2	10.6	−68.9	0.4654	(1 −1 1) [−1 −1 0]
7-1	8.4	11.0	3.8	−2.6	0.4590	(−1 1 1) [1 0 1]
8-1	24.4	88.2	16.5	−69.9	0.4520	(−1 1 1) [1 0 1]
9-1	16.6	52.7	18.5	−43.2	0.4801	(1 1 1) [1 −1 0]
10-1	3.9	6.4	27.1	−3.1	0.4272	(1 1 1) [1 −1 0]
11-1	2.8	3.6	28.1	−0.9	0.4232	(−1 1 1) [1 0 1]
12-1	2.2	6.2	20.6	−5.6	0.4233	(1 1 1) [1 −1 0]
13-1	8.4	12.7	40.9	−11.2	0.4588	(1 −1 1) [−1 −1 0]
14-1	17.7	27.7	24.5	−11.6	0.4654	(−1 1 1) [1 0 1]
15-1	6.8	74.7	5.8	−70.8	0.4429	(1 1 1) [1 −1 0]
16-1	1.7	3.5	23.7	−2.3	0.4181	(1 1 1) [1 −1 0]
1-2	2.7	84.1	2.7	−83.8	0.4265	(1 1 1) [1 −1 0]
2-2	25.6	34.2	45.0	−15.1	0.4942	(1 1 1) [1 −1 0]
3-2	14.2	13.6	24.9	0.71	0.4776	(−1 1 1) [1 0 1]
4-2	11.2	81.2	11.3	−80.2	0.4715	(1 1 1) [1 −1 0]
5-2	16.1	13.3	42.8	3.5	0.4712	(−1 1 1) [1 0 1]
6-2	39.6	56.4	49.4	−50.4	0.4595	(1 −1 1) [−1 −1 0]
7-2	15.1	40.2	23.8	−37.4	0.4837	(1 1 1) [1 −1 0]
8-2	8.7	15.3	33.8	−14.9	0.4597	(1 −1 1) [−1 −1 0]
9-2	2.8	3.9	26.5	−1.2	0.4194	(1 1 1) [1 −1 0]
10-2	13.3	12.2	16.2	1.2	0.4789	(−1 1 1) [1 0 1]
11-2	40.1	40.6	19.2	−0.48	0.4630	(−1 1 1) [1 0 1]
12-2	35.9	42.2	24.0	−7.0	0.4668	(−1 1 1) [1 0 1]
13-2	17.3	26.1	42.4	−18.7	0.4899	(1 1 1) [1 −1 0]
14-2	9.3	52.2	7.7	−44.9	0.4475	(−1 1 1) [1 0 1]
15-2	34.2	72.1	36.2	−68.7	0.4707	(1 −1 1) [−1 −1 0]
16-2	21.9	41.4	33.6	−31.8	0.4987	(1 1 1) [1 −1 0]

TABLE 2. Fractographic Results for Thermally Treated Specimens (Condition 1)

Specimen No.	Test conditions, ℃	Cycle time, s	Main crack nucleation, mm	RGZ area share, %	AGZ area share, %	N_f, cycles
1	2	3	4	5	6	7
1-1	150–900	100	First nucleus on US, second one on LS (0.1 × 0.1) turned to RGZ	50	50	3654
3-1	200–1050	178	2 nuclei on PS turned to RGZ	30	70	13
4-1	600–1050	147	Nucleus on PS (0.2 × 0.2) and multiple ones on US, RGZ (1.0 × 1.0) on PS and (0.8 × 3.0) on US	80	20	462
5-1	500–1100	34	Crack nuclei turned to RGZ	30	70	33

Table 2 continued

1	2	3	4	5	6	7
6-1	200–1100	90	Crack nucleus on PS turned to RGZ (1.0 × 2.0) with additional small nuclei on LS	30	70	40
7-1	700–1050	143	Multiple small nuclei on PS turned to RGZ (1.0 × 3.0) and (0.8 × 3.0) on US with microporosity	80	20	612
8-1	700–1050	30	Nucleus on PS (0.5 × 1.0), additional nuclei on US turned to RGZ (1.0 × 1.0)	70	30	1772
9-1	200–1100	115	Nucleus on PS (0.2 × 0.2), second nucleus on US (0.5 × 0.2)	30	70	34
10-1	150–900	143	Nucleus on PS (0.1 × 0.2)	50	50	367
11-1	500–1000	24	Multiple nuclei and pores over PS (0.2 × 0.1)	60	40	1535
12-1	200–1050	70	Nucleus on PS (0.5 × 0.5), additional nucleus on US and LS taking 20% fracture	30	70	33
13-1	500–1000	25	First nucleus on PS (0.1 × 0.1), multiple microporosity, additional nuclei on US	80	20	4137
14-1	150–900	85	Three nuclei on US (0.1 × 0.1), fusion on PS	50	50	2688
15-1	500–1100	149	Nucleus on PS (0.2 × 0.2), microporusity, additional nuclei on US and LS	50	50	141
16-1	500–1050	27	Nucleus on PS (0.1 × 0.1), three additional nuclei on LS	60	40	383

Note. Here and in Table 3: PS – polished (upper) surface, US – unpolished (lower) surface, LS – lateral surface, N_f – number of cycles to fracture.

TABLE 3. Fractographic Results for Thermally Treated Specimens (Condition 2)

Specimen No.	Test conditions, ℃	Cycle time, s	Main crack nucleation, mm	RGZ sizes and area share, mm/%	AGZ area share, %	N_f, cycles
1-2	500–1050	30	Nucleus on PS (0.1 × 0.5), pronounced microporosity	1 × 3/50	50	749
3-2	600–1100	27	Nucleus on US (0.2 × 0.5)	60	40	195
4-2	200–1100	75	Three nuclei on US (0.1 × 0.1), additional nucleus on LS (0.2 × 0.2)	20	80	30
5-2	200–1100	60	Nucleus on US (0.1 × 0.1), additional nucleus on PS (0.1 × 0.2)	0.4 × 3.0 on PS, 0.2 × 3.0 on US	50	6
7-2	150–900	70	Nucleus on PS (0.2 × 0.2)	60	40	734
8-2	200–1100	70	Nucleus on PS (0.1 × 0.2)	0.5 × 1/30	70 (fused on PS)	14
9-2	200–1050	65	Nucleus on PS (0.1 × 0.1)	0.5 × 1.5 on LS/20	80	33
10-2	500–1100	35	Nucleus on PS (0.3 × 0.2), additional nucleus on US (0.1 × 0.2) without further crack extension	1.5 × 1.0 on PS	60	50
12-2	700–1100	34	Fusion on PS and US	No RGZ, static final rupture	80	11
13-2	700–1050	20	Nucleus on PS (0.2 × 0.2), additional nucleus on LS (0.5 × 0.5)	40	60	2144
14-2	150–900	78	Nucleus on US (0.2 × 0.2)	0.5 × 0.8/30	70	1414
15-2	500–1000	39	Nucleus on PS and US turned to RGZ	10.×1.0 on PS, 0.5 × 0.8 on US	Final rupture fused	123
16-2	600–1050	30	Ditto	1.5 × 2.0 on PS, 1.0 × 2.0 on US	Ditto	376

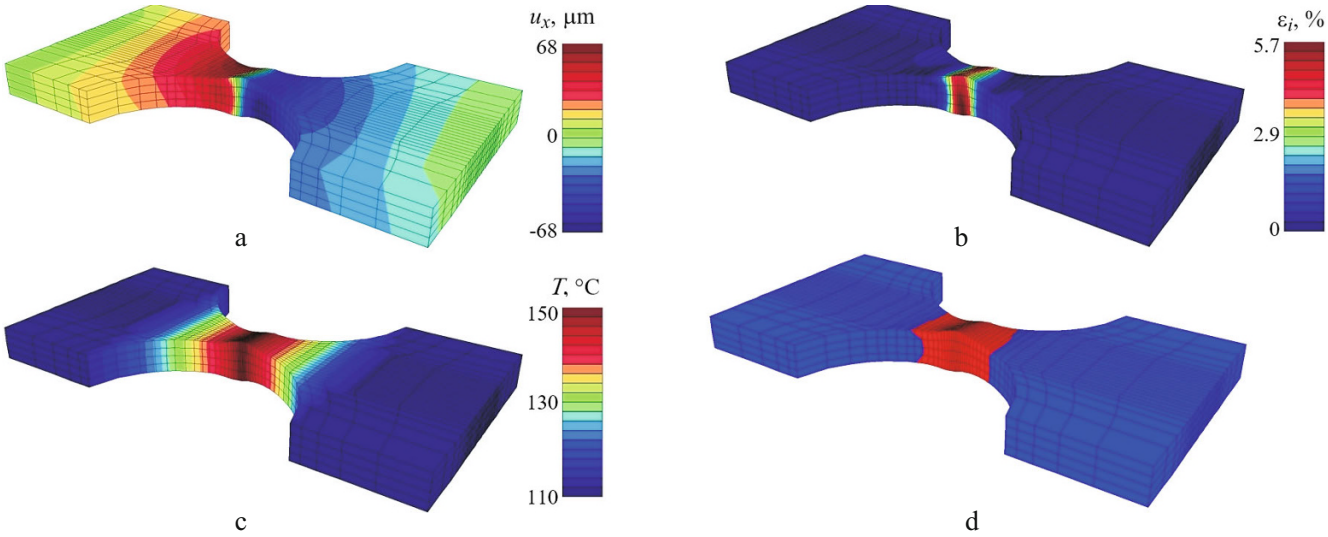

Fig. 5. Results of FE calculations for specimen No. 1-1 at T_{max} =150℃ (cooling phase) at the 10th cycle: (a), (b), (c) distributions of axial displacement, strain intensity, and temperature fields, respectively; (d) plasticity zone.

Finite Element Results. The stress-strain state assessment creates the basis for evaluating the orientation of the noncrystallographic fracture surface. The nonuniform distribution of temperature fields along the specimen, its cross-section area variations with the distance from the center, well-defined anisotropy, and temperature dependence of mechanical single-crystal properties would require numerical methods of solving the boundary problem to define nonuniform stress and strain fields. The specimen should be considered not as a material point but as a construction.

For FE calculations, micromechanical (crystallographic) models of inelastic single-crystal deformation were applied [8, 17, 18] with regard to slip systems and their interaction. The elastoplastic and viscoelastoplastic models of the material include nonlinear kinematic and isotropic hardening necessary for the adequate description of the material behavior under thermocyclic loading. The characteristics of inelastic deformation models were determined from elastoplastic deformation diagrams and creep curves of a ZhS32 alloy at different temperatures and orientations [1, 19, 20]. The 3D calculations were performed with a PANTOCRATOR FE software complex [21] capable of applying crystallographic models to a single-crystal material. The FE calculation results for specimen No. 1-1 are cited in Fig. 5.

Strain fields are localized in the central portion of the specimen. The plastic zone covers the whole central neck of the sand-glass specimen.

Typical curves of cyclic deformation for specimens No. 1-1 at 150–900℃ and No. 11-1 at 500 (T_{min})–1000℃ (T_{max}) in the central section are shown in Fig. 6. An increase in maximum cycle temperature leads to accumulation of plastic strains (for specimen No. 11-1). A wide range of temperature variations for specimen No. 1-1 results in wider hysteresis loops.

It should be noted that stress cycling is alternating-sign. In all likelihood, noncrystallographic fracture at the macrolevel would happen on the nucleation and extension of mode I cracks appearing in the cooling phase. The heating phase is accompanied by considerable compression stresses.

Among the stress tensor components, the axial one is dominating, however, unlike an isotropic material, other nonzero components are observed, making up to 30% axial ones. The normal to the surface of noncrystallographic fracture can also deflect from the specimen axis.

Identification of Fracture Modes. Assessment of a dominating (crystallographic or noncrystallographic) fracture mechanism of the specimen was based on the data of comparing the fracture line slopes on its upper and lateral surfaces with those in crystallographic analysis of slip plane traces (4), FE results for the orientation of maximum principal stress sites, and fractographic results for the fracture surface. Only RGZ cracks were investigated.

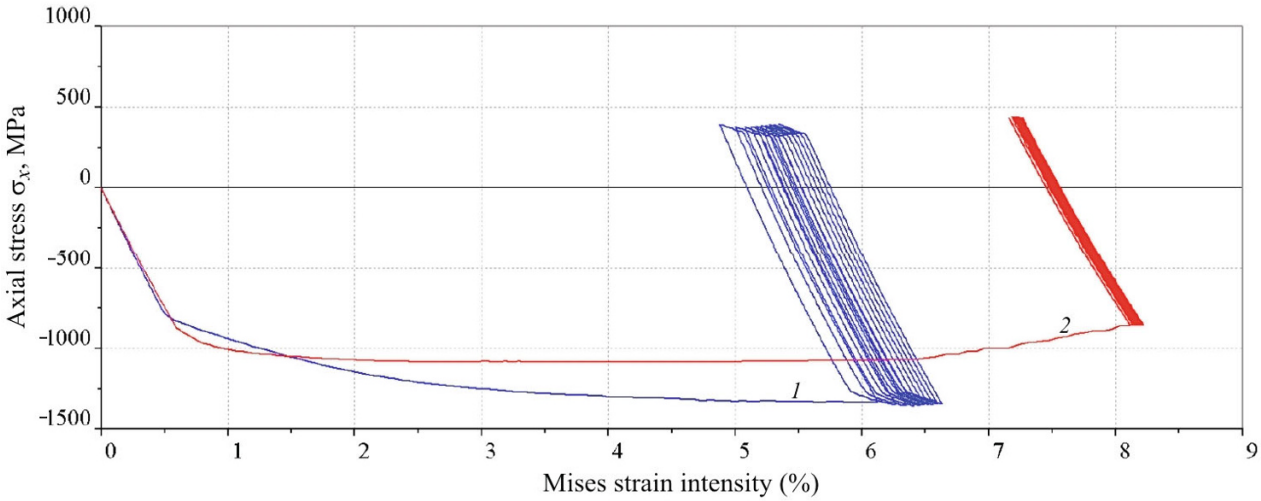

Fig. 6. Calculated curves of cyclic deformation for specimens Nos. 1-1 (*1*) and 11-1 (*2*).

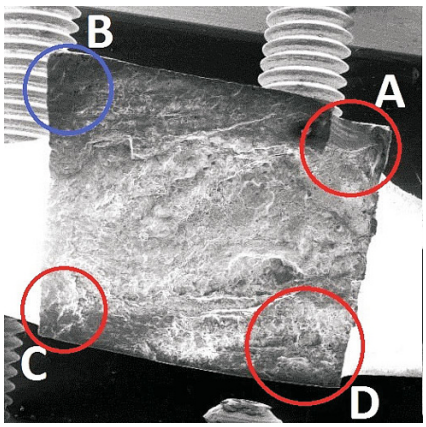

Fig. 7. Mechanisms of crystallographic (*A*, *C*, *D*) and noncrystallographic (*B*) fracture by fracture angles for specimen No. 1-1.

A final rupture zone was not examined. Four angular fracture points in Fig. 7 (*A*, *B*, *C*, *D*) were chosen as typical ones, for each of them, two fracture line slopes with respect to the specimen axis were calculated on its two adjacent sides (*XOY* and *XOZ* planes). Thus, the orientation of a fracture plane can be established in the vicinity of an examined point. The condition of crystallographic fracture in such a point is the deflection of both fracture line slopes from the slip lines, making up less than 5°. The specimen is considered to be fractured by the crystallographic mode if it is valid for all typical points in RGZ.

Comparison of fracture line slopes with those of slip lines for specimen No. 1-1 is exemplified in Table 4. In the experiment, the crack nucleus was observed in the fracture base (Fig. 7, point *C*) where the slip angles in plane (–1 1 1) with maximum Schmid factors coincide with fracture angles. The macrocrack is growing in crystallographic plane (1 1 1) (Fig. 7, points *A*, *D*) that does not coincide with the crack nucleus plane (–1 1 1). In the point *B* corresponding to the final rupture stage, the orientation of fracture lines is inconsistent with any of crystallographic planes (Fig. 7).

The plotting of points with indication of a fracture mode of specimens on the diagram, characterizing the thermocyclic loading conditions $\Delta T - T_{\max}$, permits of establishing crystallographic and noncrystallographic fracture regions with the retarded main crack growth (Fig. 8). The boundary between the regions allows for approximation of $\Delta T = A\exp(-Q/RT)$, type introduced by analogy with [6] and corresponding to the Arrhenius equation for thermoactivation processes.

TABLE 4. Fracture and Slip Line Slopes for Specimen No. 1-1

Fracture origin point in Fig. 7	Specimen side	Line slope, deg			Fracture mode
		Fracture (experiment)	Slip (crystallography)	Mode I (FE calculation)	
A	XOY	85.8	83.5	90.5	Crystallographic
	XOZ	−53.1	−58.1	−69.6	
B	XOY	83.9	83.5	88.9	Noncrystallographic (final rupture effect)
	XOZ	−36.6	−58.1	−75.0	
C	XOY	−64.2	−61.5	90.5	Crystallographic
	XOZ	53.8	51.0	−69.6	
D	XOY	84.5	83.5	88.9	
	XOZ	−54.4	−58.1	−75.0	

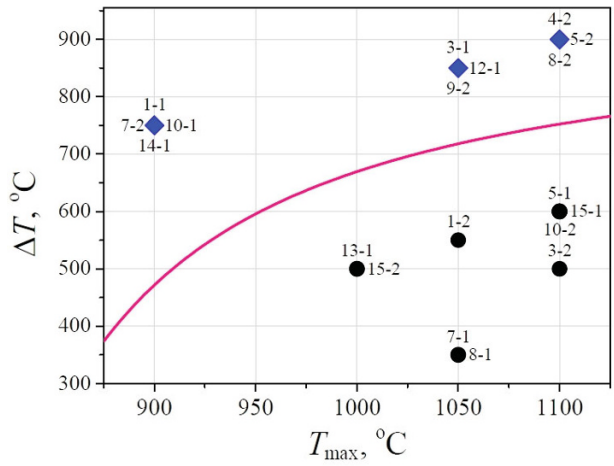

Fig. 8. Diagram of crystallographic (◆) and noncrystallographic (●) fracture mechanisms for a ZhS32 single-crystal alloy. (Figures correspond to the specimen number.)

However, in this study, the data for a well-defined boundary form are lacking.

The crystallographic mode is realized at lower maximum temperatures and a wide range of cycle temperature variations. It is characterized by combined I–II mode crack growth in crystallographic plane {111}. The noncrystallographic mode is realized at higher temperatures and narrower range of cycle temperature variations. It is characterized by mode I crack growth. Specimens fractured by the crystallographic and noncrystallographic modes are exemplified in Fig. 9. The microstructure of the fracture zone in crack-containing specimens that propagate along the slip lines and perpendicularly to the specimen axis is shown in Figs. 10 and 11.

The plotting of a fracture mechanism diagram did not consider the specimens with deflections from axial and azimuthal orientations above 20° (Fig. 8). For these specimens, a typical distribution of fracture zones becomes obscure. Specimens with large residual stresses arising at the final rupture stage were also excluded from the examination, which gives no way of determining the orientation of fracture lines with mentioned accuracy. As a result, for the plotting of a fracture mechanism diagram, 19 specimens were used (Fig. 8).

Thermal treatment conditions do not essentially influence the realization of fracture modes. Ten specimens with the crystallographic mode were tested as follows: five (condition 1) and five (condition 2). Nine specimens with the noncrystallographic mode were divided as five (condition 1) and four (condition 2).

Holding (about 2 min) at a maximum cycle temperature also does not significantly influence the fracture behavior. Of four specimens subjected to holding, two specimens (Nos. 3-1 and 10-1) and two ones (Nos. 7-1 and 15-1) corresponded to the crystallographic and noncrystallographic modes, respectively (Fig. 8).

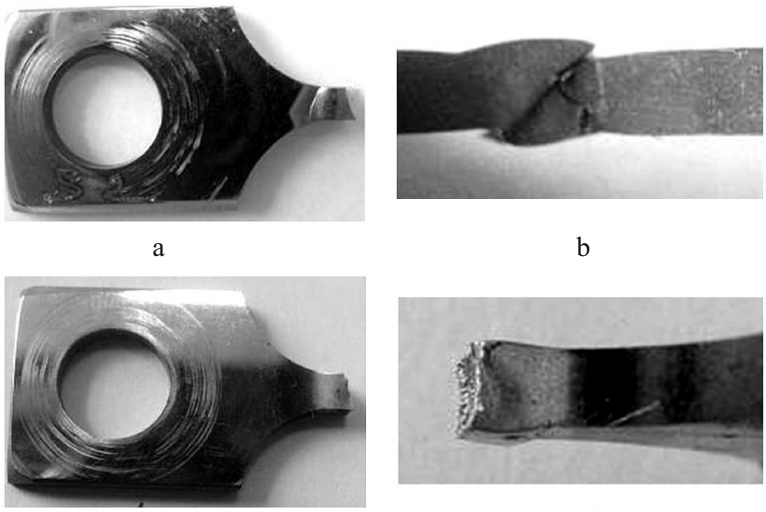

Fig. 9. External view of tested specimens Nos. 8-2 (a, b) and 8-1 (c, d) fractured by the crystallographic and noncrystallographic modes, respectively: (a, c) top view; (b, d) side view.

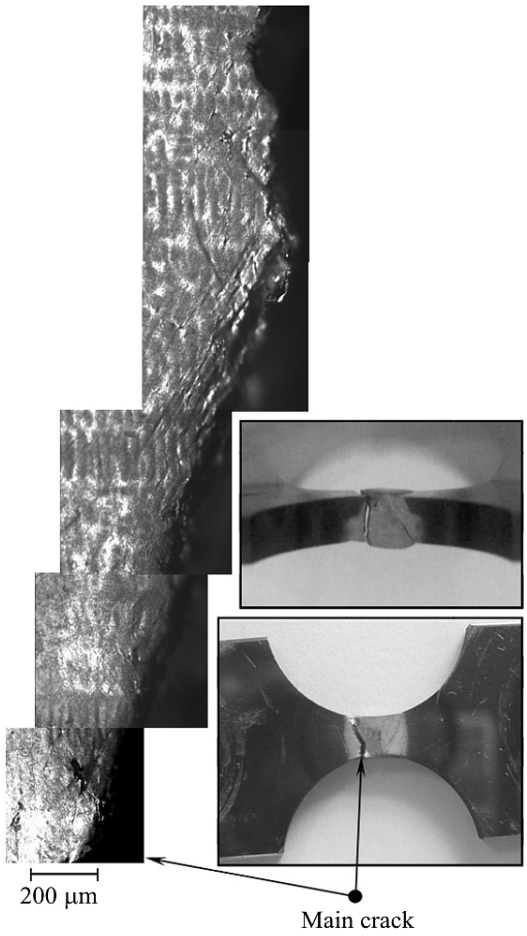

Fig. 10

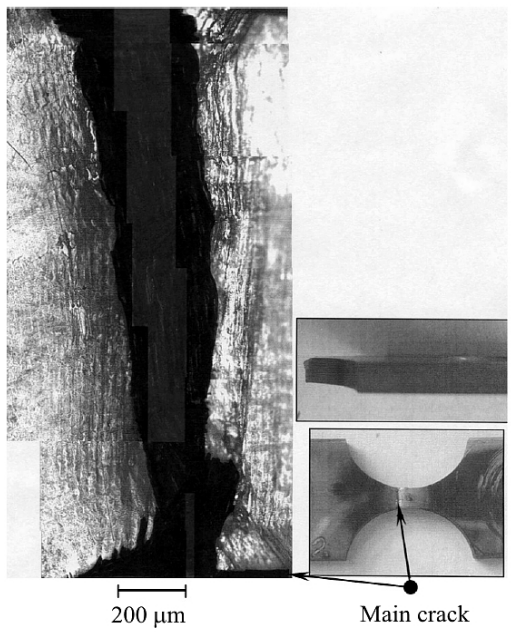

Fig. 11

Fig. 10. Micrograph of the fracture zone in specimen No. 4-1 after 462 cycles and at 600–1050℃.
Fig. 11. Micrograph of the fracture zone in specimen No. 13-2 after 2144 cycles and at 700–1050℃.

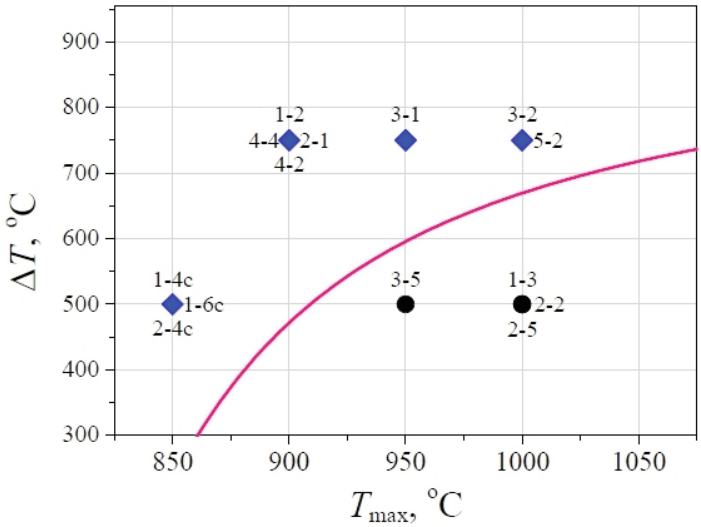

Fig. 12. Diagram of crystallographic (◆) and noncrystallographic (●) fracture mechanisms of a ZhS36 single-crystal alloy. (Figures correspond to the specimen number, test conditions and crystallographic orientation are described in [14].)

Conclusions. The fracture behavior of single-crystal alloys is characteristic of a ZhS32 carbon-bearing single-crystal alloy and a ZhS36 carbon-free one [8, 14]. The diagram of fracture mechanisms in a ZhS36 alloy for 14 specimens of different crystallographic orientations ($\langle 001 \rangle$, $\langle 011 \rangle$, $\langle 111 \rangle$) is indicative of crystallographic and noncrystallographic fracture regions (Fig. 12) with the boundary similar to that for a ZhS32 alloy (Fig. 8).

The assessment of fracture conditions on thermal fatigue corroborates the relations [6] for high-cycle fatigue at constant temperature associated with the introduction of two fracture modes of single-crystal alloys and their sensitivity to temperature and cycle amplitudes.

The study was performed with the financial support of RNF (Project No 18–19–00413).

REFERENCES

1. E. N. Kablov and E. R. Golubovskii, *Heat Resistance of Nickel Alloys* [in Russian], Mashinostroenie, Moscow (1998).
2. L. B. Getsov, V. E. Mikhailov, A. S. Semenov, et al., "Calculated life assessment of blades and guide vanes of gas turbine plants. Part 2. Single-crystal materials," *Gazoturb. Tekhnol.*, No. 8, 18–25 (2011).
3. G. R. Leverant and M. Gell, "The influence of temperature and frequency on the fatigue fracture of cube oriented nickel-base superalloy single crystals," *Metall. Trans. A*, **6**, 367–371 (1975).
4. J. Telesman and L. J. Ghosn, "The unusual near-threshold FCG behavior of a single crystal superalloy and the resolved shear stress as the crack driving force," *Eng. Fract. Mech.*, **34**, Nos. 5–6, 1183–1196 (1989).
5. J. Telesman and L. J. Ghosn, "Fatigue crack growth behavior of PWA 1484 single crystal superalloy at elevated temperatures," *J. Eng. Gas Turb. Power*, **118**, No. 2, 399–405 (1996).
6. J. Gallagher, T. Nicholas, A. Gunderson, et al., *Advanced High Cycle Fatigue (HCF) Life Assurance Methodologies*, Final Report of University of Dayton Research Institute (2004).
7. K. S. Chan, J. Feiger, Y.-D. Lee, et al., "Fatigue crack growth thresholds of deflected mixed-mode cracks in PWA1484," *J. Eng. Mater. Technol.*, **127**, No. 1, 2–7 (2005).
8. L. B. Getsov and A. S. Semenov, "Fracture criteria for polycrystalline and single-crystal materials under thermocyclic loading," in: Proc. of the TsKTI [in Russian], Issue 296 (2009), pp. 83–91.
9. L. B. Getsov, "Fracture criterion for a multiaxial loading program," in: Proc. of the All-Union Workshop on Low-Cycle Fatigue Problems [in Russian], Kaunas (1971), pp. 52–55.

10. A. S. Semenov and L. B. Getsov, “Thermal fatigue fracture criteria of single crystal heat-resistant alloys and methods for identification of their parameters,” *Strength Mater.*, **46**, No. 1, 38–48 (2014).
11. A. S. Semenov, S. G. Semenov, and L. B. Getsov, “Methods of computational determination of growth rates of fatigue, creep, and thermal fatigue cracks in poly- and monocrystalline blades of gas turbine units,” *Strength Mater.*, **47**, No. 1, 268–290 (2015).
12. E. A. Tikhomirova, A. A. Zhivushkin, L. B. Getsov, and A. I. Rybnikov, “Studies on the properties of heat-resistant nickel single-crystal superalloys,” *Vestn. Samar. Gos. Aérokosm. Univ.*, No 3, 89–97 (2011).
13. B. M. Gugelev, L. B. Getsov, Yu. N. Zhuravlev, and E. G. Novikova, “Microstructural studies on damages in metals on thermal fatigue,” *Zavod. Lab.*, No. 1, 94–98 (1976).
14. L. B. Getsov, N. I. Dobina, A. I. Rybnikov, et al., “Thermal fatigue resistance of a monocrystalline alloy,” *Strength Mater.*, **40**, No. 5, 538–551 (2008).
15. E. A. Tikhomirova, *Change of the Structure and Properties of a Casting Heat-Resistant Nickel Alloy at a Temperature-Force Effect* [in Russian], Author’s Abstract of the Candidate Degree Thesis (Tech. Sci.), Saint Petersburg (2013).
16. A. S. Semenov, *Computational Methods in the Theory of Plasticity* [in Russian], SPbGPU, Saint Petersburg (2008).
17. G. Cailletaud, “A micromechanical approach to inelastic behaviour of metals,” *Int. J. Plasticity*, **8**, No. 1, 55–73 (1991).
18. A. I. Grishchenko, A. S. Semenov, and L. B. Getsov, “Modeling inelastic deformation of single crystal superalloys with account of γ/γ' phases evolution,” *Mater. Phys. Mech.*, **24**, No. 4, 325–330 (2015).
19. L. B. Getsov, A. S. Semenov, E. A. Tikhomirova, and A. I. Rybnikov, “Failure criteria for single crystal alloys of gas turbine blades under static and thermocycling loading,” in: Proc. of the 19th Eur. Conf. on Fracture: *Fracture Mechanics for Durability, Reliability and Safety* (ECF19, August 26–31, 2012, Kazan, Russia) (2012), pp. 670–678.
20. R. E. Shalin, I. L. Svetlov, E. B. Kachanov, et al., *Single Crystals of Heat Resistant Nickel Alloys* [in Russian], Mashinostroenie, Moscow (1997).
21. A. S. Semenov, “PANTOCRATOR – finite element software complex for solving nonlinear problems of mechanics,” in: Proc. of the V Int. Conf. on Scientific-Technical Problems for Prediction of Reliability and Durability of Structures and Methods of Their Solution [in Russian], SPbGPU, Saint Petersburg (2003), pp. 466–480.